Frequency Stability-Aware Stochastic Modeling for Inter-System Bias in Multi-GNSS PPP

Jinyang Han, Jie Zhang, Shiming Zhong, Xiaolong Mi, Daqian Lyu, Runmin Lu, and Bibo Peng

***Abstract*—Global navigation satellite systems (GNSSs) exhibit differences in coordinate and time References, necessitating the consideration of inter-system bias (ISB) in multi-GNSS precise point positioning (PPP). Traditional ISB estimation models, such as white noise (ISB-WN), random walk (ISB-RW), and constant (ISB-CT) models, apply uniform Kalman filtering process noise across different receivers, precise products, and navigation systems, often neglecting ISB variations under diverse conditions. This study introduces a novel stochastic model that incorporates the frequency stability of ISB parameters (ISB-FS). By integrating the time-frequency characteristics of navigation system time references and the short-term stability of receiver hardware delays, the model employs overlapping Allan variance and a sliding window approach to adaptively update ISB process noise. An analysis involving ten stations from four manufacturers demonstrates that the ISB-FS model enhances multi-GNSS PPP solutions accuracy: positioning accuracy improves by approximately 3%, time transfer precision by 10%, and long-term frequency stability (245760 s) by up to 38%, while maintaining comparable Zenith tropospheric delay (ZTD) accuracy. This research offers a refined ISB estimation strategy, advancing the precision of multi-GNSS PPP solutions.**

***Index Terms*—Frequency stability, inter-system bias (ISB), multiglobal navigation satellite system (GNSS), precise point positioning (PPP).**

NOMENCLATURE

GNSS	Global navigation satellite system.
PPP	Precise point positioning.
ISB	Inter-system bias.
RW	Random walk.
WN	White noise.
CT	Constant.
ZTD	Zenith tropospheric delay.
MGEX	Multi-GNSS experiment.
IGS	International GNSS service.
E, *N*, and *U*	East, north, and up.
IF	Ionosphere free.
DOY	Doy of year.
MDEV	Modified Allan variance.
G, *R*, *E*, and *C*	GPS, GLONASS, Galileo, and BDS.

I. INTRODUCTION

WITH the continuous development of navigation and positioning systems, the number of visible satellites worldwide has greatly increased [1], [2], [3]. Research into the application of multi-GNSS signals to obtain precise positioning, navigation, and timing (PNT) is rapidly growing in the scientific community [4], [5], [6]. Multi-GNSS PPP not only guarantees high geometric strength but also significantly accelerates PPP initialization and increases solution accuracy [7], [8], [9].

However, owing to the differences in coordinates and time references for different satellite systems and variations in receiver hardware delays, ISB must be considered in the multi-GNSS PPP model solutions [10], [11], [12].

Many researchers have analyzed the characteristics of ISB parameters. Torre and Caporali [13] reported that different receivers introduce specific biases for specific GNSS systems. Zhou et al. [14] found that ISB is related not only to receiver types but also to differences in GNSS time references in clock bias products. Liu et al. [15] reported that ISB is stable within one day, whereas jumps occur between adjacent days and are related to the reference changes in MGEX clock products.

Regarding ISBs parameter estimation methods, the candidate strategies mainly include the white noise (ISB-WN), RW (ISB-RW), and CT (ISB-CT) models. Li and Zhang [16] suggested that for Center for Orbit Determination in Europe (CODE) and Wuhan University (WHU) products, the ISB-CT model provides better positioning accuracy and convergence speed than the ISB-RW and ISB-WN models. However, for GFZ products, the performance of the ISB-CT model is inferior. Liu et al. [17] reported that the ISB-CT model causes decimeter-level positioning errors at some stations and concluded that the ISB-RW model outperforms both the

Received 1 March 2025; revised 7 May 2025; accepted 29 May 2025. Date of publication 9 June 2025; date of current version 26 June 2025. This work was supported in part by the National Natural Science Foundations of China under Grant 42174222, in part by Wuhan Knowledge Innovation Special Project under Grant 2023010201010082, in part by the Equipment Development Project of Chinese Academy of Sciences under Grant YJKYYQ20190062, and in part by the National Key Research and Development Program of China under Grant 2023YFF0713505-4. The Associate Editor coordinating the review process was Dr. Alessio De Angelis. *(Corresponding authors: Jie Zhang; Daqian Lyu.)*

Jinyang Han and Runmin Lu are with the Innovation Academy for Precision Measurement Science and Technology, Chinese Academy of Sciences, Wuhan 430071, China, and also with the College of Earth and Planetary Sciences, University of Chinese Academy of Sciences, Beijing 101408, China (e-mail: goldensun_han@apm.ac.cn; lurunmin@apm.ac.cn).

Jie Zhang and Shiming Zhong are with the Innovation Academy for Precision Measurement Science and Technology, Chinese Academy of Sciences, Wuhan 430071, China (e-mail: zhangjie@apm.ac.cn; smzhong@apm.ac.cn).

Xiaolong Mi is with the Department of Land Surveying and Geo-Informatics, The Hong Kong Polytechnic University, Hong Kong, China (e-mail: xiaolong.mi@polyu.edu.hk).

Daqian Lyu is with the College of Electronic Engineering, National University of Defense Technology, Hefei 230037, China (e-mail: daqian_lv@nudt.edu.cn).

Bibo Peng is with the National Geodetic Observatory, Innovation Academy for Precision Measurement Science and Technology, Chinese Academy of Sciences, Wuhan 430077, China (e-mail: pengbibo@apm.ac.cn).

Digital Object Identifier 10.1109/TIM.2025.3577851

ISB-CT and ISB-WN models in terms of accuracy and convergence speed.

On the basis of the analysis, the ISB-RW model is commonly used for ISB parameter estimation, whereas the RW noise in ISB-RW models is fixed [4], [15], [18]; however, in-depth research has not been conducted for specific receivers, precise products, and navigation systems. To address this, Mikoś et al. [19], [20] explored the effects of different types of process noise on multi-GNSS PPP solutions and suggested that appropriate process noise in multi-GNSS PPP leads to slight improvements in the North (N) and East (E) directions, but significant improvements in the up (U) direction and short-term frequency stability for time transfer. Therefore, a reasonable model for defining the process noise of ISB parameter estimation in different scenarios is also worth exploring.

On the basis of the above analysis, this article considers the time-frequency characteristics of ISB parameters and proposes a stochastic model that considers the frequency stability of ISB parameters (ISB-FS). The ISB-FS model sets the process noise by calculating the overlapping Allan variance (ADEV) of the ISB and updates the process noise adaptively using a sliding window. This article first introduces the observation model of multi-GNSS PPP and the composition of the ISB parameters. Section II analyzes the characteristics of the ISB parameters, and on the basis of the above analysis, the principles of the ISB-FS model are introduced. Section III presents the selection of experimental stations, the data processing strategies, and the accuracy evaluation method. Finally, the conclusions are summarized, and the results show that the ISB-FS model has improved positioning accuracy, time transfer precision, and medium-to long-term frequency stability compared with the existing ISB parameter estimation models, with a computed ZTD accuracy similar to that of the existing models.

II. METHODOLOGY

In this section, the principles of multi-GNSS kinematic PPP, the composition of the ISB parameters, and the model for estimating the ISB parameters are introduced.

A. Multi-GNSS PPP Observations

The observation equation for dual-frequency ionosphere-free (IF) combined multi-GNSS PPP can be written as follows [21]:

$$\begin{aligned} P^s_{r,\mathrm{IF}_{ij}} &= \mu^s_r \cdot x_r + c\overline{dt}^G_r + \mathrm{ISB}^{R,E,C} + \mathrm{M}w^s_r \cdot Z_r + \varepsilon^s_{r,\mathrm{IF}_{ij}} \\ L^s_{r,\mathrm{IF}_{ij}} &= \mu^s_r \cdot x_r + c\overline{dt}^G_r + \mathrm{ISB}^{R,E,C} + \mathrm{M}w^s_r \cdot Z_r \\ &\quad + \bar{N}^s_{r,\mathrm{IF}_{ij}} + \xi^s_{r,\mathrm{IF}_{ij}} \end{aligned} \tag{1}$$

where the superscript s represents the satellite number; G, R, E, and C represent the GPS, GLONASS, Galileo, and BDS systems, respectively; the subscript r denotes the receiver ID number; the subscripts i and j denote the two frequencies used in the IF combination; μ^s_r represents the direction cosine; x_r represents the 3-D position of the receiver; c denotes the speed of light; $c\overline{dt}^G_r$ denotes the receiver clock offset for the GPS system; $\mathrm{ISB}^{R,E,C}$ denotes the ISB of other navigation systems relative to the GPS system; $\mathrm{M}w^s_r$ represents the wet delay mapping function, which can be obtained through the global mapping function (GMF) [22]; Z_r denotes the zenith tropospheric wet delay; $\bar{N}^s_{r,\mathrm{IF}}$ denotes the integer ambiguity after parameter recombination; $P^s_{r,\mathrm{IF}}$ and $L^s_{r,\mathrm{IF}}$ denote the observations of the pseudorange and carrier, respectively. $\varepsilon^s_{r,\mathrm{IF}}$ and $\xi^s_{r,\mathrm{IF}}$ denote the observation noise of the pseudorange and carrier, respectively. Notably, satellite orbits and clock offsets are corrected by the final satellite orbits and clock offset products, the tropospheric hydrostatic delay is corrected by Saastamoinen model, and the differential code bias (DCBs) is corrected by the Chinese Academy of Sciences (CASs) products [23]. Thus, for simplicity, they are omitted from (1).

After parameter recombination, the receiver clock offset and ISB can be expressed as follows:

$$\begin{cases} c\overline{dt}^G_r = cdt^G_r + b^G_{r,\mathrm{IF}} \\ \mathrm{ISB}^{E,C} = cdt^{E,C}_r - cdt^G_r + b^{E,C}_{r,\mathrm{IF}} - b^G_{r,\mathrm{IF}} \\ \mathrm{ISB}^R = cdt^R_r - cdt^G_r + b^R_{r,\mathrm{IF}} - b^G_{r,\mathrm{IF}} + \mathrm{IFCB}^R_{r,\mathrm{IF}} \end{cases} \tag{2}$$

where $dt^{G,R,E,C}_r$ represents the receiver clock for each navigation system; $b^{G,R,E,C}_{r,\mathrm{IF}}$ represents the IF combined receiver pseudorange bias for each navigation system, and $\mathrm{IFCB}^R_{r,\mathrm{IF}}$ represents the IF combined interfrequency code bias for the GLONASS system.

In (2), the difference between the receiver clocks of the two systems can also be represented

$$cdt^{R,E,C}_r - cdt^G_r = \mathrm{Time}^{R,E,C} - \mathrm{Time}^G + D_{\mathrm{MGEX}} \tag{3}$$

where $\mathrm{Time}^{R,E,C}$ represents the time reference of each GNSS (GNSS-T) and D_{MGEX} represents the time reference bias introduced by the use of MGEX precise clock products, which is related to the precise product. Notably, the MGEX is a global initiative led by the IGS to extend GNSS tracking and analysis capabilities. Through a worldwide network of multi-GNSS monitoring stations, MGEX provides high-precision products, including satellite orbits, clock corrections, and signal quality assessments. By substituting (3) into (2), the expression for the ISB parameters can be derived

$$\begin{cases} \mathrm{ISB}^{E,C} = \mathrm{Time}^{E,C} - \mathrm{Time}^G + D_{\mathrm{MGEX}} + b^{E,C}_{r,\mathrm{IF}} - b^G_{r,\mathrm{IF}} \\ \mathrm{ISB}^R = \mathrm{Time}^R - \mathrm{Time}^G + D_{\mathrm{MGEX}} + b^R_{r,\mathrm{IF}} \\ \qquad - b^G_{r,\mathrm{IF}} + \mathrm{IFCB}^R_{r,\mathrm{IF}}. \end{cases} \tag{4}$$

B. Stochastic Models of ISB

PPP usually uses Kalman filtering for parameter estimation [24]. For ISB parameters, three models currently commonly used for parameter estimation: the ISB-WN model, the ISB-CT model, and the ISB-RW model. The parameter estimation strategies for each model also differ. For the ISB-WN model, the ISB parameters are considered uncorrelated and independent between epochs and are treated as WN for estimation. The Kalman filter prediction state equation and process noise can be expressed as follows [24], [25]:

$$\begin{cases} \hat{\mathrm{ISB}}^{R,E,C}(k) = \mathrm{ISB}^{R,E,C}_{\mathrm{SPP}}(k) \\ Q^{R,E,C}_{\mathrm{ISB,WN}}(k) = q^2_{\mathrm{WN}} \end{cases} \tag{5}$$

where k represents the current epoch, $\hat{\mathrm{ISB}}^{R,E,C}(k)$ represents the ISB predicted for each system at epoch k, $\mathrm{ISB}_{\mathrm{SPP}}^{R,E,C}(k)$ represents the ISBs of each system obtained via the Standard point positioning (SPP) at epoch k, $Q_{\mathrm{ISB,WN}}^{R,E,C}(k)$ represents the process noise of the clock of each system at epoch k, and q_{WN}^2 represents the spectral density of the WN, which is generally given as 100^2 m^2 on the basis of empirical values [26].

Considering the small short-term variation and relative stability of ISB parameters, many researchers have also considered the interepoch constraints and proposed modeling approaches. The commonly used modeling methods are ISB-RW and ISB-CT models. Its Kalman filter prediction state equation and process noise can be expressed as [27]

$$\begin{cases}\hat{\mathrm{ISB}}^{R,E,C}(k) = \mathrm{ISB}^{R,E,C}(k-1)\\ Q_{\mathrm{ISB,RW}}^{R,E,C}(k) = q_{\mathrm{RW}}^2 \cdot \tau\\ Q_{\mathrm{ISB,CT}}^{R,E,C}(k) = 0\end{cases} \tag{6}$$

where τ represents the current epoch; $Q_{\mathrm{ISB,RW}}^{R,E,C}(k)$ and $Q_{\mathrm{ISB,CT}}^{R,E,C}(k)$ represent the process noise of the ISB-RW and ISB-CT models at epoch k, respectively; and q_{RW}^2 represents the spectral density of the ISB-WN model, generally given as 10^{-6} m^2/s on the basis of empirical values [16]. For the ISB-CT model, the ISB parameters are assumed to be CT and have the same value between epochs; thus, its process noise is set to 0 m^2 [10].

III. ANALYSIS OF ISB CHARACTERISTICS

As shown in (4), the ISB parameters are related to the satellite navigation systems, the precise products, and the receiver type. In this section, four MGEX stations are chosen to analyze the ISB parameters for different satellite navigation systems, different stations, different organization precise products, and the long-term characteristics of the ISB parameters. Notably, the ISB results we analyze are obtained on the basis of the ISB-WN model, and since the ISB absorbs the pseudorange bias of each satellite navigation system, the magnitude of its array varies. For better analysis, we set the first epoch of the computed results to 0.

A. ISB Parameters for Different Satellite Navigation Systems

Fig. 1 presents the ISB parameters for different satellite navigation systems at the four stations. The figure shows that the ISB parameters exhibit high short-term stability, with daily variations of less than 1 ns. The ISB parameters for different satellite navigation systems differ at the subnanosecond level. At the IENG station, the ISB fluctuation trend is similar for the three systems, but the ISB parameters of C system differ from those of the other two systems. At the ONS1 station, the ISB variation trends of the R and E systems are similar, but the ISB trend of C system differs from those of the other two systems. At the MATE and BRUX stations, the fluctuation trends of the E and C systems are similar, whereas the fluctuations of the R system differ from those of the other systems.

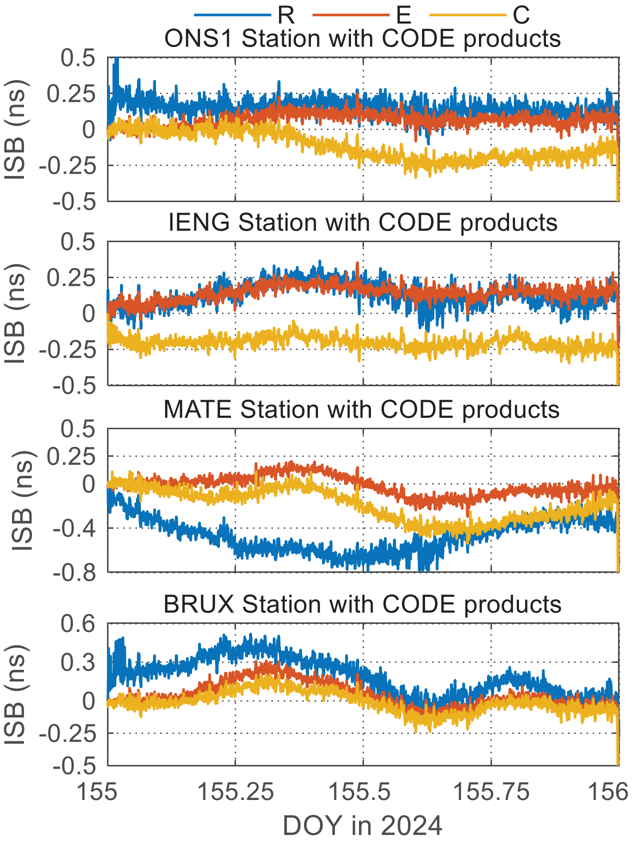

Fig. 1. ISB values for different satellite navigation systems (blue: R; red: E; yellow: C) at ONS1, IENG, MATE, and BRUX stations on DOY 155, 2024.

B. ISB Parameters for Different Stations

Fig. 2 shows the ISB values for different stations in the same navigation system. The results indicate that there are subnanosecond level differences in the ISB values of the same navigation system across the four stations. The ISB fluctuation trends at the IENG and ONS1 stations are similar across the three systems, with the ISB differences between the two stations being within 0.2 ns. For the MATE station, the ISB fluctuation trends for the E and C systems are similar to those for the BRUX station, with the ISB difference between the two stations being within 0.1 ns for the E system and within 0.2 ns for the C system. For the R system, the ISB values at the IENG and MATE stations differ significantly from those at the other stations, by up to 0.5 ns.

C. ISB Parameters for the Precision Products of Different Organizations

Fig. 3 shows the ISB values calculated for the precision products of different organizations at four stations. The results indicate that the ISB values for the precision products of different organizations all differ. The ISB values calculated via CODE, GRG, and WUM products exhibit subnanosecond-level differences, whereas the ISB differences between the IAC products and the other organizations products are at the nanosecond level. The ISB fluctuation trends for the GRG, CODE, and WUH organization products are similar, fluctuating within the range of −0.5 to 0.5 ns. However, the

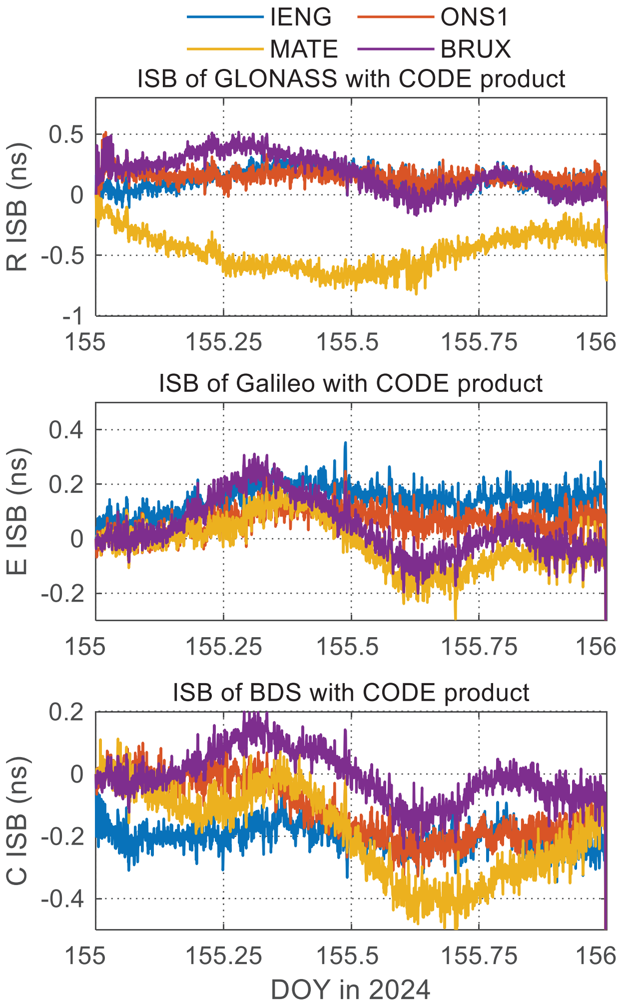

Fig. 2. ISB values for different stations (blue: IENG, red: ONS1, orange: MATE, and purple: BRUX) with the same satellite navigation system on DOY 155, 2024.

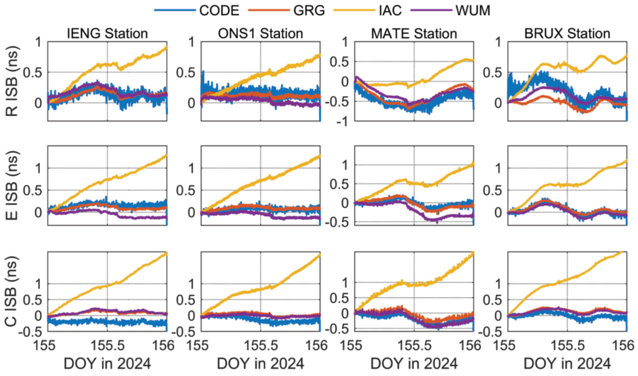

Fig. 3. ISB values calculated for different precision products (blue: CODE; red: GRG; yellow: IAC; purple: WUM) at the IENG, ONS1, MATE, and BRUX stations on DOY 155, 2024.

ISB values for the *R* system calculated via the CODE products present significantly more noise. The ISB values calculated by the IAC products clearly show a trend, with differences at the nanosecond level compared with the other organizations. The large difference may be due to the different satellite clock handling strategies used by the IAC compared with those used by the other organizations.

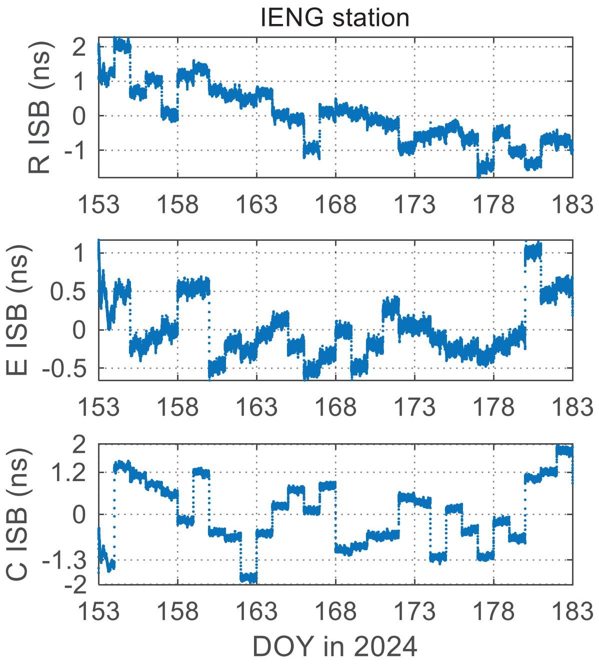

Fig. 4. ISB values of the *R*, *E*, and *C* satellite navigation systems at the IENG station on DOY 153–183, 2024.

D. Long-Term Characteristics of ISB

Fig. 4 shows the 30-day ISB values at the IENG station. The calculated ISB values exhibit irregular daily jumps at the nanosecond level, with each system showing different jump patterns. It should be noted that these daily jumps can be attributed to the processing strategy of the satellite clock offset products we employed, which involves daily batch processing [28] and consequently introduces these periodic jumps in ISB values. Among these systems, *C* System exhibits the most pronounced jump magnitude, with a notable 2.6-ns discontinuity observed on day of year (DOY) 154, 2024. Although the *R* and *E* systems show fewer jumps, there are also jumps greater than 1 ns on certain days.

On the basis of the above analysis, the ISB is relatively stable within a day. However, there are subnanosecond-level ISB differences for different satellite navigation systems, different stations, and the precision products of different organizations, and irregular jumps at the nanosecond level occur at the day boundaries. Therefore, it is more appropriate to assign suitable process noise to ISB parameters on the basis of different scenarios.

IV. STOCHASTIC MODEL OF FREQUENCY STABILITY IN ISB

The ISB parameter represents the time reference bias between two satellite navigation systems [29]. Since GNSS-T is maintained by high-precision atomic clocks [30], [31], the frequency stability analysis method is retained to describe the characteristics of the ISB parameters. The process noise

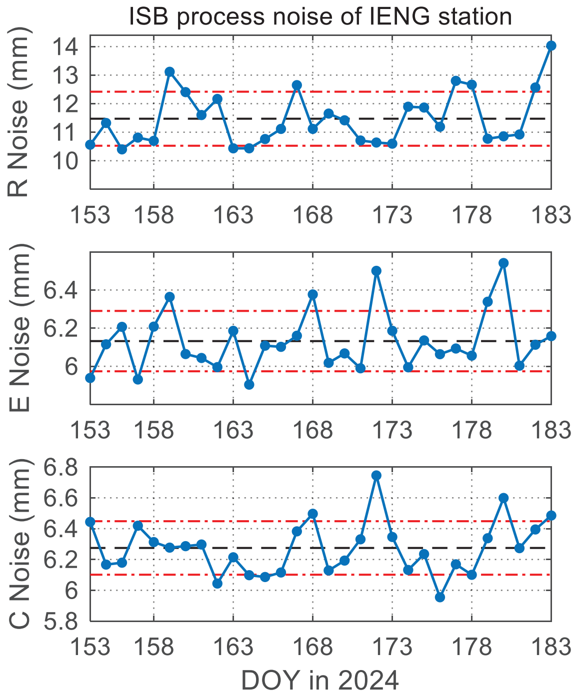

Fig. 5. IENG station process noise values of the R, E, and C navigation systems calculated via the ISB-FS model on DOY 153–183, 2024.

is specified by calculating the overlapping ADEV of the ISB parameters. Consequently, the Kalman filter prediction state equation and process noise can be expressed as follows:

$$\begin{cases} \hat{\mathrm{ISB}}_r^{R,E,C}(k) = \mathrm{ISB}_r^{R,E,C}(k-1) \\ Q_{\mathrm{ISB,FSC}}^{R,E,C}(k) = (\mathrm{ADEV}(\tau)\cdot c\cdot\tau)^2 \end{cases} \tag{7}$$

where $Q_{\mathrm{ISB,FSC}}^{R,E,C}(k)$ represents the process noise of the ISB-FS models at epoch k and $\mathrm{ADEV}(\tau)$ represents the overlapping ADEV at an interval of τ, which can be expressed as follows [32]:

$$\mathrm{ADEV}^2(\tau) = \frac{1}{2(N-2m)\tau^2}\sum_{i=1}^{N-2m}\left[x_{i+2m} - 2x_{i+m} + x_i\right]^2 \tag{8}$$

where x_i denotes the ISB values, N is the total number of ISB parameters, and m is the smoothing factor.

Fig. 5 shows the process noise calculated daily at the IENG station via the ISB-FS model. The daily process noise values show small variations. The ISB values of the R system change by approximately 4 mm over 30 days, whereas the changes for the E and C systems are all within 1 mm, indicating that the ISBs process noise estimated using the ISB-FS model is relatively stable within a day.

As mentioned in the above section, the ISB values exhibits day-boundary jumps, and Fig. 5 shows that the ISB process noise of the ISB-FS model is relatively stable. Therefore, a sliding window is applied to update the process noise. The process noise is calculated from the ISB values obtained the previous day and then applied to calculate the current ISB values. Fig. 6 provides a schematic of updating the ISB process noise on the basis of the sliding window.

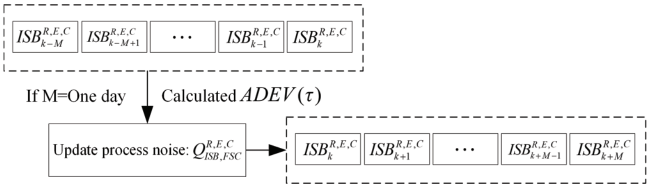

Fig. 6. Schematic of updating the ISB-FS model parameters on the basis of a sliding window.

TABLE I
DETAILS OF THE SELECTED STATIONS

Manufacture	Station	Location	Receiver	Antenna
Trimble	BOR1	Poland	TRIMBLE NETR9	TRM59800.00
	ONS1	Sweden	TRIMBLE ALLOY	LEIAR25.R3
SEPT	BRUX	Belgium	SEPT POLARX5TR	JAVRINGANT_DM
	USN7	USA	SEPT POLARX5TR	TPSCR.G5
	USN8	USA	SEPT POLARX5TR	TPSCR.G5
	USUD	Japan	SEPT POLARX5	AOAD/M_T
	IENG	Italy	SEPT POLARX4TR	SEPCHOKE_MC
Javad	GODN	USA	JAVAD TRE_3 DELTA	TPSCR.G3
Leica	MATE	Italy	LEICA GR30	LEIAR20
	WTZR	Germany	LEICA GR50	LEIAR25.R3

V. EXPERIMENTAL STRATEGIES

We first introduce the details of the MGEX stations selected for the experiment, then explain the different parameter estimation strategies, and finally present the accuracy evaluation methods for the different estimation parameters.

A. Data Selection

In this experiment, we selected ten MGEX stations from four different receiver manufacturers for the experiment (available at https://cddis.nasa.gov/archive/gps/data/daily/2024/). Detailed information about the selected stations is shown in Table I. Notably, except for the USN7 and USN8 stations, the receiver and antenna types for the other stations are all different, the USN7 and USN8 stations share one same antenna, forming a zero-baseline link, and both stations are externally connected to a coordinated universal time [UTC (USNO)] clock source. For the positioning and ZTD experiments, the experimental date were obtained from DOY 154 to 157 in 2024, over a period of three days. For the time transfer experiments, the experimental date was obtained from DOY 153 to 183 in 2024, over a period of 30 days. The data interval for all the experiments was 30 s.

B. Data Processing Strategy

The GNSS parameter estimation software was developed by modifying RTKLIB (available at https://www.rtklib.com/), and the results were analyzed and visualized in MATLAB.

TABLE II
DATA PROCESSING STRATEGY AND ACCURACY ASSESSMENT REFERENCE

Item	Models/strategies
Constellation	GPS(L1/L2) ,GLONASS(G1/G2) ,Galileo(E1/E5a) ,BDS(B1I/B3I)
Observable model	IF combination
Satellite orbit and clock	Final IAC products
Data Format	RINEX
Cutoff mask angle	7.5°
Weighting	Elevation weighting
Filtering method	Extended Kalman filter
Antenna correction	igs20.atx
Tides	Solid tides, ocean tide, pole tide
Earth rotation	IGS ERP products [33]
Relativistic effect	Corrected [34]
Phase windup effect	Corrected [35]
Satellite and receiver DCB	CAS products [23]
Troposphere hydrostatic delay	Saastamoinen [36]
Station coordinates	CT estimation
Receiver clock	WN estimation (10^4 m^2)
ISBs	WN/CT/RW (10^{-6} m^2/s)/FS estimation
Troposphere wet delay	RW estimation (9×10^{-6} m^2/s)
Integer ambiguity	CT estimation
Station coordinates reference	SNX files [37]
Clock reference	Zero baseline and common clock strategy [38]
Troposphere reference	Final IGS products

The data processing strategy for the experiment is detailed in Table II. Notably, the ISB parameters were estimated via the ISB-WN model, the ISB-RW model, the ISB-CT model, and the ISB-FS model proposed in this article, and all the day experimental data from one station were processed with a single filter.

It should be noted that all related products and files listed in Table II can be obtained from https://cddis.nasa.gov/archive/gps/products/. We evaluate the accuracy and robustness of the ISB-FS model from three aspects: positioning, clock offset, and ZTD parameters. To evaluate the accuracy of both positioning and ZTD parameters, we adopted the following reference standards: 1) station coordinates derived from solution independent exchange (SNX) files processed by the IGS, representing the highly accurate positional solutions and 2) final ZTD products from IGS. The positioning and ZTD accuracies were quantitatively assessed by computing root mean square (rms) values between our solutions and these reference datasets. For the clock bias parameters, USN7-USN8 is a zero-baseline and shares the same clock source, which allows for the removal of clock source errors and results in CT time transfer between the two stations. Since we did not perform hardware delay calibration, we subtracted the mean of the time transfer results during data analysis. The experiment assesses the time transfer precision by calculating the standard deviation (STD) of the time transfer results and evaluates the frequency stability by analyzing the MDEV. The MDEV can be expressed as follows [32]:

$$H_{\mathrm{MDEV}}^2(\tau) = \frac{1}{2m^2(N-3m+1)\tau^2} \times \sum_{j=1}^{N-3m+1}\left\{\sum_{i=j}^{j+m-1}\left[x_{i+2m} - 2x_{i+m} + x_i\right]\right\}^2 \tag{9}$$

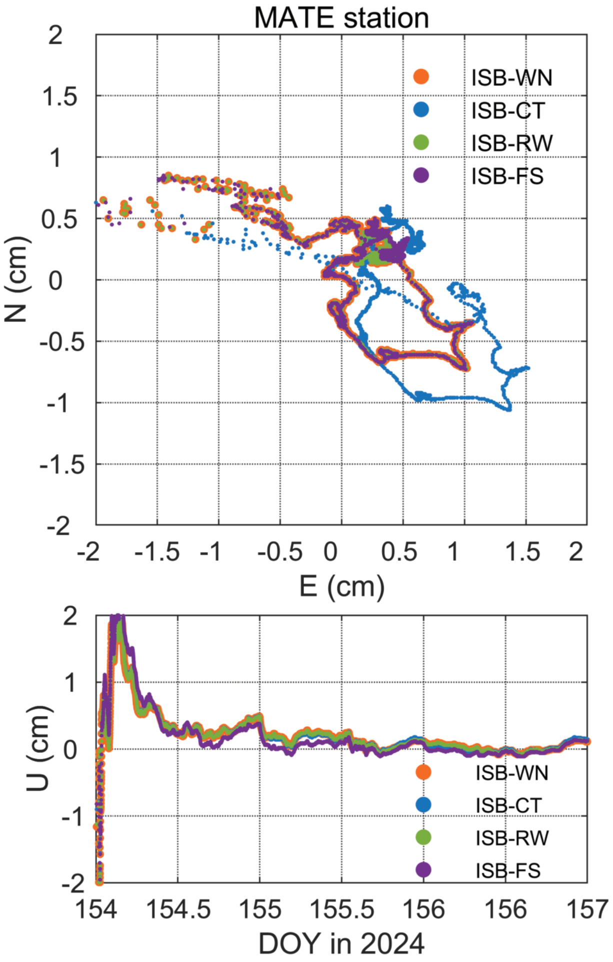

Fig. 7. Positioning error distributions of the MATE station calculated via the ISB-WN, ISB-CT, ISB-RW, and ISB-FS models on DOY 154–157, 2024.

where $H_{\mathrm{MDEV}}(\tau)$ represents the MDEV at an interval of τ, x_i denotes the clock bias values, N is the total number of clock biases, and m is the smoothing factor.

VI. RESULTS AND ANALYSIS

In this section, we analyze the accuracy of the ISB-FS model from three perspectives: positioning, time transfer, and ZTD parameters. Since there is no quantitative definition but only qualitative definitions of long-term, medium-term, and short-term stability in the field of time and frequency, and the definitions of long-term, medium-term, and short-term stability for different types of atomic clocks are different. To facilitate subsequent time transfer frequency stability analysis, short-term frequency stability is notably defined as the stability before 1000 s. Stability within the time span of 1000–10000 s is referred to as medium-term frequency stability, whereas the stability after 10000 s is termed long-term frequency stability.

A. Analysis of Positioning Results

Fig. 7 presents the positioning error of the MATE station, where the upper figure shows the horizontal (E and N) positioning error, and the lower figure shows the U positioning

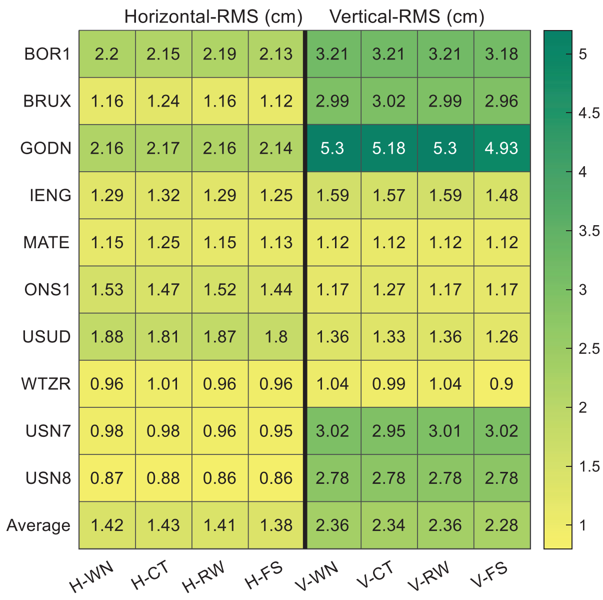

	Horizontal-RMS (cm)				Vertical-RMS (cm)			
	H-WN	H-CT	H-RW	H-FS	V-WN	V-CT	V-RW	V-FS
BOR1	2.2	2.15	2.19	2.13	3.21	3.21	3.21	3.18
BRUX	1.16	1.24	1.16	1.12	2.99	3.02	2.99	2.96
GODN	2.16	2.17	2.16	2.14	5.3	5.18	5.3	4.93
IENG	1.29	1.32	1.29	1.25	1.59	1.57	1.59	1.48
MATE	1.15	1.25	1.15	1.13	1.12	1.12	1.12	1.12
ONS1	1.53	1.47	1.52	1.44	1.17	1.27	1.17	1.17
USUD	1.88	1.81	1.87	1.8	1.36	1.33	1.36	1.26
WTZR	0.96	1.01	0.96	0.96	1.04	0.99	1.04	0.9
USN7	0.98	0.98	0.96	0.95	3.02	2.95	3.01	3.02
USN8	0.87	0.88	0.86	0.86	2.78	2.78	2.78	2.78
Average	1.42	1.43	1.41	1.38	2.36	2.34	2.36	2.28

Fig. 8. RMS values of the positioning results calculated via the ISB-WN, ISB-CT, ISB-RW, and ISB-FS models on DOY 154–157, 2024.

error. The horizontal positioning accuracy of the ISB-CT model is inferior to those of other three models, likely because the ISB-CT model does not align with the ISB characteristics. From the rms perspective, except for the ISB-CT model with a horizontal positioning rms of 1.25 cm, the positioning accuracies of the ISB-WN and ISB-RW models are approximately 1.15 cm. Among them, the ISB-FS model has the highest accuracy, reaching 1.13 cm, which is approximately 10%–2% greater than those of the ISB-CT and ISB-RW models, respectively. The *U* positioning accuracies of all four strategies are nearly the same.

Fig. 8 presents the rms values for ten stations and the average horizontal and *U* rms values for the stations. With respect to the station average rms, the ISB-FS model has the highest accuracy, with the horizontal accuracy improved by approximately 3%, 4%, and 2% compared with those of the ISB-WM, ISB-CT, and ISB-RW models, respectively. The elevation accuracy improved by approximately 3% overall compared with those of the three models. Taking the comparison between the ISB-FS and ISB-RW models as an example, the horizontal accuracy at the ONS1 station shows the most significant improvement, with the rms decreasing from 1.52 to 1.44 cm, a 4% improvement. The *U* accuracy at the GODN station shows the greatest improvement, with the rms decreasing from 5.30 to 4.93 cm, a 7% improvement.

B. Analysis of Time Transfer Results

Fig. 9 presents the time transfer and frequency stability results for the USN7-USN8 link. For better distinction, the time transfer results of the ISB-WN and ISB-RW models are adjusted. The results of the ISB-CT model show considerable jitter, possibly because the CT model does not align with the ISB parameter characteristics, causing the related errors to be absorbed by the receiver clock. The results of the other three models follow a similar trend. The time transfer of the ISB-FS model is significantly smoother and exhibits less jitter, and the daily jump on DOY 178 is smaller than those of the other two models, suggesting that the ISB-FS model can improve the discontinuity at the daily boundary. The time transfer STDs of the ISB-FS model are 39.7 ps, 13%, 83%, and 16% lower than the STDs of 45.5, 226.5, and 47.3 ps for the ISB-WN, ISB-CT, and ISB-RW model results, respectively.

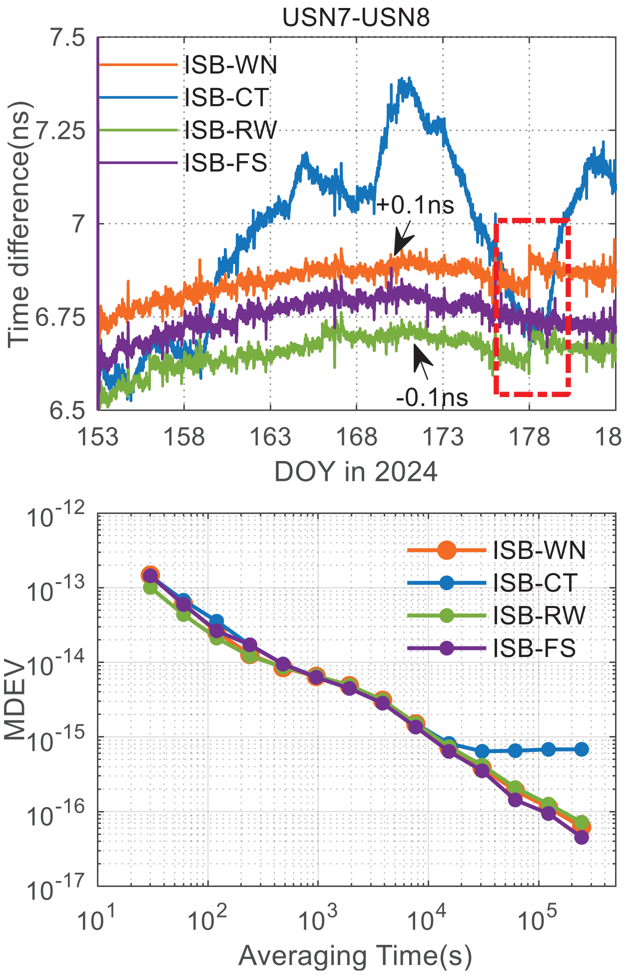

Fig. 9. Time differences and MDEVs of the USN7-USN8 link calculated via the ISB-WN, ISB-CT, ISB-RW, and ISB-FS models on DOY 153–183, 2024.

With respect to frequency stability, except for the ISB-CT model, the 100-s frequency stability of the other models reaches the 10^{-14} region, and the 200000-s frequency stability reaches the 10^{-17} region. Fig. 10 shows the ratio of improvement of the ISB-FS model compared with the other three models. Among them, the ISB-RW model has higher short-term stability, whereas the ISB-FS model shows significantly better middle- and long-term stability than the existing models. Taking the comparison between the ISB-FS and ISB-RW models as an example, the short-term frequency stability results of the ISB-FS model are inferior to those of the ISB-RW model, and the 30-s stability increases from 1.01×10^{-13} to 1.44×10^{-13}, representing a decrease of 43%. However, as the sampling interval increases, the results of the two models

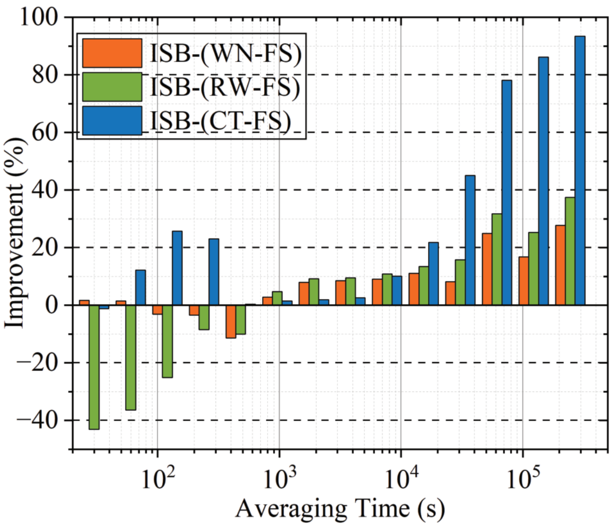

Fig. 10. Frequency stability improvement ratios of the ISB-FS model compared with those of the ISB-WN, ISB-CT, and ISB-RW models on DOY 153–183, 2024.

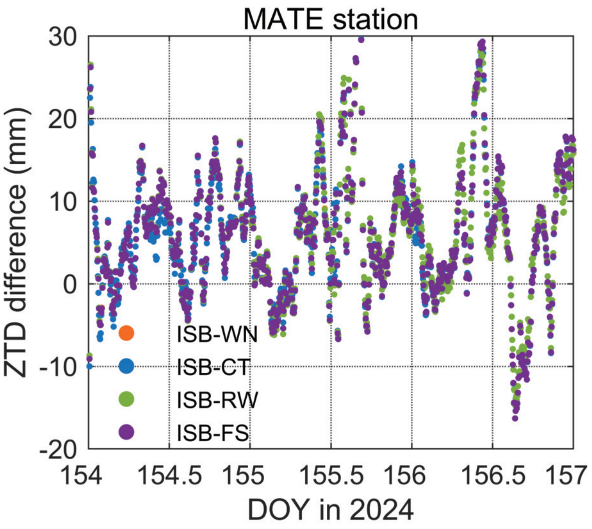

Fig. 11. ZTD differences for the MATE station compared with the IGS products determined via the ISB-WN, ISB-CT, ISB-RW, and ISB-FS models on DOY 154–157, 2024.

gradually converge, and the 960-s stability decreases from 6.38×10^{-15} to 6.29×10^{-15}, representing an improvement of 1%. The mid-term frequency stability of the ISB-FS model is slightly better than that of the ISB-RW model, and the 76800-s stability decreases from 1.51×10^{-15} to 1.35×10^{-15}, representing an improvement of 11%. The long-term frequency stability of the ISB-FS model is also slightly better than that of the ISB-RW model, with overall improvements exceeding 10%. The most significant improvement is observed at 245760 s, where the frequency stability decreases from 7.20×10^{-17} to 4.50×10^{-17}, representing an improvement of 38%. This indicates that the ISB-FS model has higher mid-term and long-term frequency stability than the ISB-WN, ISB-CT, and ISB-RW models, respectively.

C. Analysis of ZTD Results

Fig. 11 presents the ZTD difference results for the MATE station. The figure shows that the ZTD results from the four models have comparable accuracies and correspond well with the IGS final products, with peak-to-peak values all within 50 mm. Fig. 12 shows the rms values of the ZTD differences for all the stations and the station average. For the MATE and USN8 stations, the rms calculated by the four models is greater than 10 mm, while for the other stations, the RMSs are all less than 10 mm. The ISB-WN and ISB-RW models have similar accuracies, with average station RMSs of 6.92 and 6.93 mm, respectively. The average station rms for the ISB-FS model is 7.01 mm, which is approximately 1% lower than that of the ISB-WM model. The slightly lower accuracy of the ISB-FS model may be due to the added constraints on the ISB parameters, which result in some unmodeled errors being absorbed by the ZTD parameters.

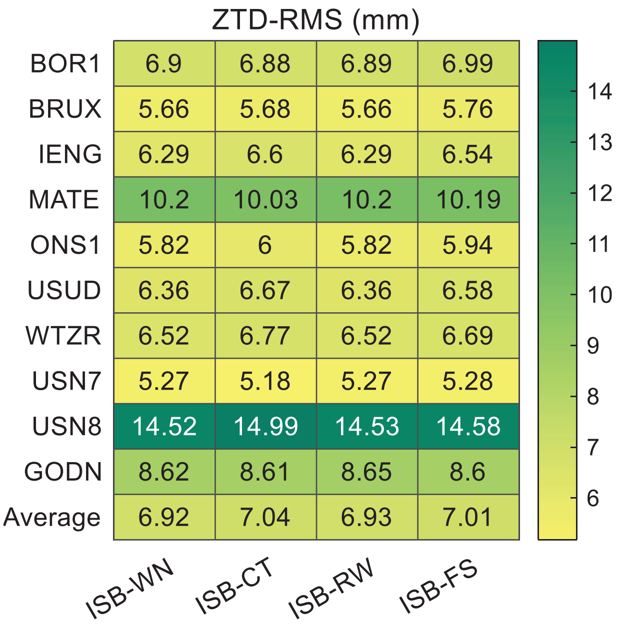
ZTD-RMS (mm)

	ISB-WN	ISB-CT	ISB-RW	ISB-FS
BOR1	6.9	6.88	6.89	6.99
BRUX	5.66	5.68	5.66	5.76
IENG	6.29	6.6	6.29	6.54
MATE	10.2	10.03	10.2	10.19
ONS1	5.82	6	5.82	5.94
USUD	6.36	6.67	6.36	6.58
WTZR	6.52	6.77	6.52	6.69
USN7	5.27	5.18	5.27	5.28
USN8	14.52	14.99	14.53	14.58
GODN	8.62	8.61	8.65	8.6
Average	6.92	7.04	6.93	7.01

Fig. 12. RMS values of the ZTD results calculated via the ISB-WN, ISB-CT, ISB-RW, and ISB-FS models on DOY 154–157, 2024.

As can be seen from Figs. 8, 9, and 12, the ISB parameter estimation model significantly impacts time transfer. When the ISB parameter estimation model is set to a CT model, the time transfer results exhibit obvious distortion, whereas the positioning and ZTD accuracy remain largely unaffected.

VII. CONCLUSION

This study investigates the characteristics of ISB parameters and introduces a stochastic model that incorporates the frequency stability of these parameters. The ISB-FS model is compared with three existing models (ISB-WN, ISB-RW, and ISB-CT) in terms of multi-GNSS PPP solutions accuracy, including positioning, time transfer, and ZTD estimation. The detailed conclusions are as follows.

The differences in ISB parameters between different receivers and different satellite navigation systems are at the subnanosecond level, whereas the differences between different precision products are at the subnanosecond to nanosecond level. Additionally, there are irregular nanosecond-level jumps in the ISB parameters at the daily boundary, and the jumps differ between different satellite navigation systems.

The ISB-FS model improves positioning accuracy by approximately 3% compared to the ISB-WN, ISB-RW, and ISB-CT models. Time transfer precision is enhanced by 13%, 83%, and 16% compared to the ISB-WN, ISB-RW, and ISB-CT models, respectively. In terms of frequency stability, the ISB-FS model shows slightly lower short-term performance but significantly better mid-term and long-term stability, with improvements of up to 11% and 38%, respectively. The ZTD accuracy of the ISB-FS model is comparable to that of the existing models.

This study primarily evaluates the robustness of the ISB-FS model using static data from geodetic receivers. In practical applications, especially with low-cost receivers and dynamic environments, the short-term variations in receiver hardware delays may be more complex [39]. Future research should focus on assessing the robustness of the ISB-FS model across diverse environments and receiver types to ensure its applicability in various practical scenarios.

APPENDIX

Here, to enhance readability, we provide explanations for frequently used abbreviations in nomenclature

ACKNOWLEDGMENT

The authors would like to thank the international GNSS service (IGS), Chinese Academy of Science (CAS), and CDDIS for providing related products. The authors also appreciate the reviewers for their valuable suggestions on improving the manuscript.

REFERENCES

[1] C. J. Hegarty and E. Chatre, "Evolution of the global navigation SatelliteSystem (GNSS)," *Proc. IEEE*, vol. 96, no. 12, pp. 1902–1917, Dec. 2008, doi: 10.1109/JPROC.2008.2006090.

[2] J. Blanch, T. Walter, and P. Enge, "Satellite navigation for aviation in 2025," *Proc. IEEE*, vol. 100, no. 5, pp. 1821–1830, May 2012, doi: 10.1109/JPROC.2012.2190154.

[3] R. T. Ioannides, T. Pany, and G. Gibbons, "Known vulnerabilities of global navigation satellite systems, status, and potential mitigation techniques," *Proc. IEEE*, vol. 104, no. 6, pp. 1174–1194, Jun. 2016, doi: 10.1109/JPROC.2016.2535898.

[4] Z. Ma et al., "Influence of inter-system biases on combined single-frequency BDS-2 and BDS-3 pseudorange positioning of different types of receivers," *Remote Sens.*, vol. 16, no. 10, p. 1710, May 2024, doi: 10.3390/rs16101710.

[5] C. Shi, Y. Hu, F. Zheng, and D. Zhang, "Accounting for BDS-2/BDS-3 inter-system biases in PPP and RTK models," *Adv. Space Res.*, vol. 70, no. 4, pp. 890–906, Aug. 2022, doi: 10.1016/j.asr.2022.05.030.

[6] J. M. Juan et al., "Enhanced precise point positioning for GNSS users," *IEEE Trans. Geosci. Remote Sens.*, vol. 50, no. 10, pp. 4213–4222, Oct. 2012, doi: 10.1109/TGRS.2012.2189888.

[7] M. Elsheikh, A. Noureldin, and M. Korenberg, "Integration of GNSS precise point positioning and reduced inertial sensor system for lane-level car navigation," *IEEE Trans. Intell. Transp. Syst.*, vol. 23, no. 3, pp. 2246–2261, Mar. 2022, doi: 10.1109/TITS.2020.3040955.

[8] A. Rovira-Garcia, J. M. Juan, J. Sanz, and G. González-Casado, "A worldwide ionospheric model for fast precise point positioning," *IEEE Trans. Geosci. Remote Sens.*, vol. 53, no. 8, pp. 4596–4604, Aug. 2015, doi: 10.1109/TGRS.2015.2402598.

[9] X. Li et al., "High-rate GPS seismology using real-time precise point positioning with ambiguity resolution," *IEEE Trans. Geosci. Remote Sens.*, vol. 52, no. 10, pp. 6165–6180, Oct. 2014, doi: 10.1109/TGRS.2013.2295373.

[10] R. Tu et al., "Multiple GNSS inter-system biases in precise time transfer," *Meas. Sci. Technol.*, vol. 30, no. 11, Sep. 2019, Art. no. 115003, doi: 10.1088/1361-6501/ab32b3.

[11] X. Mi, C. Sheng, A. El-Mowafy, and B. Zhang, "Characteristics of receiver-related biases between BDS-3 and BDS-2 for five frequencies including inter-system biases, differential code biases, and differential phase biases," *GPS Solutions*, vol. 25, no. 3, pp. 1–11, Jun. 2021, doi: 10.1007/s10291-021-01151-w.

[12] X. Mi, B. Zhang, Y. Yuan, and X. Luo, "Characteristics of GPS, BDS2, BDS3 and Galileo inter-system biases and their influence on RTK positioning," *Meas. Sci. Technol.*, vol. 31, no. 1, Jan. 2020, Art. no. 015009, doi: 10.1088/1361-6501/ab4209.

[13] A. D. Torre and A. Caporali, "An analysis of intersystem biases for multi-GNSS positioning," *GPS Solutions*, vol. 19, no. 2, pp. 297–307, Apr. 2015, doi: 10.1007/s10291-014-0388-2.

[14] F. Zhou, D. Dong, P. Li, X. Li, and H. Schuh, "Influence of stochastic modeling for inter-system biases on multi-GNSS undifferenced and uncombined precise point positioning," *GPS Solutions*, vol. 23, no. 3, pp. 1–13, Jul. 2019, doi: 10.1007/s10291-019-0852-0.

[15] T. Liu, Y. Yuan, B. Zhang, N. Wang, B. Tan, and Y. Chen, "Multi-GNSS precise point positioning (MGPPP) using raw observations," *J. Geodesy*, vol. 91, no. 3, pp. 253–268, Oct. 2016, doi: 10.1007/s00190-016-0960-3.

[16] P. Li and X. Zhang, "Integrating GPS and GLONASS to accelerate convergence and initialization times of precise point positioning," *GPS Solutions*, vol. 18, no. 3, pp. 461–471, Oct. 2013, doi: 10.1007/s10291-013-0345-5.

[17] X. Liu, W. Jiang, P. Li, Z. Deng, M. Ge, and H. Schuh, "An extended inter-system biases model for multi-GNSS precise point positioning," *Measurement*, vol. 206, Jan. 2023, Art. no. 112306, doi: 10.1016/j.measurement.2022.112306.

[18] Y. Shi, B. Lian, Y. Zeng, Y. Ma, and Y. Liu, "Spatiotemporal calibration based on nonlinear optimization for heterogeneous information including GNSS raw data," *IEEE Trans. Veh. Technol.*, vol. 74, no. 5, pp. 7099–7113, May 2025, doi: 10.1109/TVT.2024.3521402.

[19] M. Mikoş, K. Kazmierski, T. Hadas, and K. Sośnica, "Stochastic modeling of the receiver clock parameter in galileo-only and multi-GNSS PPP solutions," *GPS Solutions*, vol. 28, no. 1, pp. 1–15, Jan. 2024, doi: 10.1007/s10291-023-01556-9.

[20] M. Mikoś, K. Kazmierski, T. Hadas, and K. Sośnica, "Multi-GNSS PPP solutions with different handling of system-specific receiver clock parameters and inter-system biases," *GPS Solutions*, vol. 27, no. 3, pp. 1–14, Jul. 2023, doi: 10.1007/s10291-023-01474-w.

[21] A. Leick, L. Rapoport, and D. Tatarnikov, *GPS Satellite Surveying*. Hoboken, NJ, USA: Wiley, 2015.

[22] J. Boehm, A. Niell, P. Tregoning, and H. Schuh, "Global mapping function (GMF): A new empirical mapping function based on numerical weather model data," *Geophys. Res. Lett.*, vol. 33, no. 7, pp. 1–4, Apr. 2006, doi: 10.1029/2005gl025546.

[23] J. Han, J. Zhang, S. Zhong, B. Peng, R. Lu, and C. Zhou, "The effect of satellite code bias on GPS PPP time transfer," *J. Spatial Sci.*, vol. 70, no. 1, pp. 29–44, May 2024, doi: 10.1080/14498596.2024.2349552.

[24] L. Tang, J. Wang, B. Cui, H. Zhu, M. Ge, and H. Schuh, "Multi-GNSS precise point positioning with predicted orbits and clocks," *GPS Solutions*, vol. 27, no. 4, pp. 1–15, Oct. 2023, doi: 10.1007/s10291-023-01499-1.

[25] X. Mi, B. Zhang, A. El-Mowafy, K. Wang, and Y. Yuan, "Undifferenced and uncombined GNSS time and frequency transfer with integer ambiguity resolution," *J. Geodesy*, vol. 97, no. 2, pp. 1–13, Feb. 2023, doi: 10.1007/s00190-022-01689-8.

[26] C. Fan, Z. Yao, S. Wang, and J. Xing, "Pseudolite system-augmented GNSS real-time kinematic PPP," *J. Geodesy*, vol. 96, no. 10, pp. 1–12, Oct. 2022, doi: 10.1007/s00190-022-01663-4.

[27] M. Mikoś, K. Kazmierski, and K. Sośnica, "Characteristics of the IGS receiver clock performance from multi-GNSS PPP solutions," *GPS Solutions*, vol. 27, no. 1, pp. 1–13, Jan. 2023, doi: 10.1007/s10291-023-01394-9.

[28] X. Zhang et al., "Influence of precise products on the day-boundary discontinuities in GNSS carrier phase time transfer," *Sensors*, vol. 21, no. 4, p. 1156, Feb. 2021, doi: 10.3390/s21041156.

[29] P. Defraigne and J.-M. Sleewaegen, "Code-phase clock bias and frequency offset in PPP clock solutions," *IEEE Trans. Ultrason., Ferroelectr., Freq. Control*, vol. 63, no. 7, pp. 986–992, Jul. 2016, doi: 10.1109/TUFFC.2015.2501350.

[30] G. Petit, "Sub-10–16 accuracy GNSS frequency transfer with IPPP," *GPS Solutions*, vol. 25, no. 1, pp. 1–9, Jan. 2021, doi: 10.1007/s10291-020-01062-2.

[31] X. Mi, B. Zhang, A. El-Mowafy, K. Wang, and Y. Yuan, "On the potential of undifferenced and uncombined GNSS time and frequency transfer with integer ambiguity resolution and satellite clocks estimated," *GPS Solutions*, vol. 27, no. 1, pp. 1–12, Nov. 2022, doi: 10.1007/s10291-022-01363-8.

[32] W. J. Riley, "Handbook of frequency stability analysis," Nat. Inst. Standards Technol., Boulder, CO, USA, NIST Special Publiccation 1065, 2008.

[33] G. Petit and B. Luzum, "The 2010 reference edition of the IERS conventions," in *Reference Frames for Applications in Geosciences*. Berlin, Germany: Springer, 2013.

[34] J. Kouba, "A guide to using International GNSS Service (IGS) products," Geodetic Surv. Division, Natural Resour. Canada, Tech. Rep., 2009.

[35] J. T. Wu, S. C. Wu, G. A. Hajj, W. I. Bertiger, and S. M. Lichten, "Effects of antenna orientation on GPS carrier phase," *Manuscripta Geodaetica*, vol. 18, no. 2, pp. 91–98, Feb. 1993.

[36] J. Saastamoinen, "Contributions to the theory of atmospheric refraction," *Bull. Géodésique*, vol. 105, no. 1, pp. 279–298, Sep. 1972.

[37] O. O. Khoda, "Estimation of velocities of Ukrainian GNSS stations in the IGb08 reference frame," *Kinematics Phys. Celestial Bodies*, vol. 40, no. 5, pp. 257–268, Oct. 2024, doi: 10.3103/s0884591324050039.

[38] J. Han, J. Zhang, S. Zhong, R. Lu, and B. Peng, "PPP time transfer using an adaptive clock constraint model," *Geo-Spatial Inf. Sci.*, pp. 1–13, Oct. 2024, doi: 10.1080/10095020.2024.2408333.

[39] X. Mi, B. Zhang, R. Odolinski, and Y. Yuan, "On the temperature sensitivity of multi-GNSS intra- and inter-system biases and the impact on RTK positioning," *GPS Solutions*, vol. 24, no. 4, pp. 1–14, Aug. 2020, doi: 10.1007/s10291-020-01027-5.

Jinyang Han is currently pursuing the Ph.D. degree with the State Key Laboratory of Precision Geodesy, Innovation Academy for Precision Measurement Science and Technology, Chinese Academy of Sciences (CAS), Wuhan, China.

His current research mainly focuses on multi-GNSS PPP time transfer algorithm and its application in dynamic.

Jie Zhang is an Associate Researcher with the State Key Laboratory of Precision Geodesy, Innovation Academy for Precision Measurement Science and Technology, Chinese Academy of Sciences (CAS), Wuhan, China. His current research focuses on high-precision time and frequency transfer and its applications and satellite laser ranging.

Shiming Zhong is an Associate Professor with the State Key Laboratory of Precision Geodesy, Innovation Academy for Precision Measurement Science and Technology, Chinese Academy of Sciences (CAS), Wuhan, China. His research interests focus on satellite orbit determination, GNSS precise point positioning, and SLR data processing.

Xiaolong Mi received the dual Ph.D. degrees from the University of Chinese Academy of Sciences, Beijing, China, and Curtin University, Perth, WA, Australia, in 2022 and 2023, respectively.

He is currently a Research Assistant Professor with the Department of Land Surveying and Geo-Informatics, The Hong Kong Polytechnic University, Hong Kong. His research interests include GNSS and low Earth orbit (LEO) technologies for positioning, navigation, and timing (PNT) along with the application of artificial intelligence (AI) in Earth and space sciences.

Daqian Lyu is a Lecturer with the College of Electronic Engineering, National University of Defense Technology, Hefei, China. His current research interests include GNSS precise positioning and time transfer.

Runmin Lu is currently pursuing the Ph.D. degree with the State Key Laboratory of Geodesy and Earth Dynamics, Innovation Academy for Precision Measurement Science and Technology, Chinese Academy of Sciences (CAS), Wuhan, China.

His current research mainly focuses on GNSS time transfer and its applications.

Bibo Peng is a Professor and a Doctoral Supervisor with the State Key Laboratory of Precision Geodesy, Innovation Academy for Precision Measurement Science and Technology, Chinese Academy of Sciences (CAS), Wuhan, China. His current research mainly focuses on space geodesy and geodynamics.